The Astrophysical Journal, 935:128 (9pp), 2022 August 20 https://doi.org/10.3847/1538-4357/ac8164

CARAMEL-GAS: A Step toward Fast Empirical Models of the Broad-line-emitting Gas

Peter R. Williams and Tommaso Treu[1]
Department of Physics and Astronomy, University of California, Los Angeles, CA 90095-1547, USA; pwilliams@astro.ucla.edu
Received 2022 May 16; revised 2022 July 5; accepted 2022 July 13; published 2022 August 23

Abstract

Fast empirical models of the broad emission line region (BLR) are a powerful tool to interpret velocity-resolved reverberation mapping (RM) data, estimate the mass of the supermassive black holes, and gain insight into its geometry and kinematics. Much of the effort so far has been devoted to describing the emissivity of one emission line at a time. We present here an alternative approach aimed at describing the underlying BLR gas distribution, by exploiting simple numerical recipes to connect it with emissivity. This approach is a step toward describing multiple emission lines originating from the same gas and allows us to clarify some issues related to the interpretation of RM data. We illustrate this approach—implemented in the code CARAMEL-GAS—using three data sets covering the Hβ emission line (Mrk 50, Mrk 1511, Arp 151) that have been modeled using the emissivity-based version of the code. As expected, we find differences in the parameters describing the BLR gas and emissivity distribution, but the emissivity-weighted lag measurements and all other model parameters including black hole mass and overall BLR morphology and kinematics are consistent with the previous measurements. We also model the Hα emission line for Arp 151 using both the gas- and emissivity-based BLR models. We find ionization stratification in the BLR with Hα arising at larger radii than Hβ, while all other model parameters are consistent within the uncertainties.

Unified Astronomy Thesaurus concepts: Supermassive black holes (1663); Astronomy data modeling (1859); Photoionization (2060); Reverberation mapping (2019)

1. Introduction

In recent years, the quality and quantity of velocity-resolved reverberation mapping data has increased dramatically. These high-quality data sets provide unique insights into supermassive black holes and their surrounding gas, which is responsible for the broad emission lines defining Type I active galactic nuclei (AGNs) and known as the broad-line region (BLR). On the one hand they can be used to determine black hole masses at arbitrary distances (e.g., Williams et al. 2021b). On the other hand they can be used to characterize the overall morphology and kinematics of the broad-line-emitting gas, which is generally too compact to be angularly resolved (but see recent GRAVITY results; Gravity Collaboration et al. 2018, 2020, 2021). In turn, characterizing the morphology and kinematics of the BLR improves the precision and accuracy of black hole mass measurements using reverberation mapping and also indirect estimates based on single-epoch spectra. Furthermore, even a simple phenomenological description of the BLR can help us understand the physical processes at work in the immediate vicinity of active supermassive black holes. Extracting this valuable information from velocity-resolved reverberation mapping data requires, inevitably, some degree of modeling.

One approach to determining black hole mass and BLR geometry and kinematics consists of forward modeling the reverberation mapping data directly, as first proposed by Pancoast et al. (2011) and Brewer et al. (2011). The current implementation of this method is now known as the modeling code CARAMEL. In this approach, the geometry and kinematics of the BLR, the gravitational effects of the black hole, and the continuum light curves are described with simple but flexible phenomenological models. The simplicity of the models is driven by the requirement to compute them fast enough to perform a statistical inference on the data with finite computational resources. In practice, one has to be able to compute model predictions millions of times. Even on highly parallelized supercomputers this means that only very simple phenomenological models can be implemented at the moment, and this should be kept in mind when interpreting any result. The errors associated with the inferred parameters account for both measurement errors and residual mismatches between the data and the best models. The latter are generally dominant since the signal-to-noise ratio of the data is usually very high.

A lot has been learned by applying CARAMEL to high-quality data for 17 AGNs. First, black hole masses are typically inferred with 0.1–0.2 dex uncertainty. Second, the comparison of inferred black hole masses with the so-called virial product yields a direct estimate of the virial coefficient, which is on average in very good agreement with that inferred by assuming that the $M_{\rm BH}$–σ relation is the same for active and inactive galaxies. Third, the broad-line region appears to be generally described by disks or tori seen close to face-on, as expected for Type I AGNs. Fourth, no clear pattern has been found to describe the kinematics, which appear to be a mixture of inflow, outflow, and bound gas, perhaps akin to "weather." Application of CARAMEL to data sets taken over multiple years (Pancoast et al. 2018) or with multiple lines (Williams et al. 2020) builds confidence that key parameters such as black hole mass and overall morphological features are robust.

New data sets covering multiple emission lines bring opportunities for improved measurements of BLR properties, and perhaps more accurate and precise estimates of black hole mass. For example, emission lines of the same species arise

[1] Packard Fellow.

from the same gas in the BLR and are inherently connected by the common gravitational potential and by the physics of photoionization. In its current state, CARAMEL only models the BLR emission and has no way of connecting two emission line data sets for the same AGN. The comparison and combination can only be done a posteriori (Williams et al. 2020).

Rather than modeling the BLR emission that we see, one could model the BLR gas itself and include in the model a description of how the gas distribution translates to gas emission. In principle, such a model could describe one universal distribution of BLR gas, and photoionization calculations would predict which regions of that gas emit the different emission lines we observe. This would allow for simultaneous modeling of multiple emission lines for a single AGN, further improving measurements of the black hole mass and BLR properties. However, such a detailed treatment is at the moment computationally unfeasible within an inference scheme.

In this paper, we take a step toward carrying out inferences of reverberation mapping data using gas-based BLR models, by presenting a new version of the code CARAMEL. For clarity we will refer to the gas-based version as CARAMEL-GAS and the emissivity-based version as CARAMEL-LIGHT.

The reasons for making these changes are as follows. First, we wish to address a limitation of CARAMEL-LIGHT—that it does not fit the absolute flux scale of the observed emission lines and instead includes a scaling factor to match the continuum and emission line strengths. There is a reason to allow for arbitrary rescaling of the emission line, namely that we do not have access to the ionizing continuum light curve. However, this has raised some concern that the fitted BLR models are not able to reproduce the total emission line luminosity in physical units. By introducing physics to describe the reprocessing of energy, we can ensure that the models are capable of producing the observed flux in the emission lines. Second, as more high-quality data sets come out covering multiple emission lines (e.g., NGC 5548 and Mrk 817; De Rosa et al. 2015; Kara et al. 2021), we have the opportunity improve BLR parameter measurements by fitting more than one emission line at once.

Due to the computational limitation mentioned above, the changes described in this paper cannot use full photoionization models, but rely on functional forms connecting gas and its emissivity that are meant to mimic the full calculations while allowing for sufficient freedom via a set of free parameters. We use a simple power law in this first step, but future model development could include more complex functions such as broken power laws with inner and outer radii. We also do not simultaneously model multiple emission lines at this stage since we first need to assess how the CARAMEL-GAS results compare to the CARAMEL-LIGHT results. Additional development will be needed to incorporate multiple emission lines.

We apply CARAMEL-GAS to a selection of data that have already been modeled with CARAMEL-LIGHT with two overall aims. First, we aim to characterize the morphology and kinematics of the gas and test the robustness of measurements of supermassive black hole mass and inferences of the overall geometry and kinematics by comparing the results obtained with the two codes. Second, by modeling a system for which both Hα and Hβ have been monitored, we derive some of the general implications of these models in terms of physics of the BLR.

The paper is organized as follows. In Section 2, we describe CARAMEL-GAS and the differences with respect to CARAMEL-LIGHT. In Section 3, we apply CARAMEL-GAS to two AGNs from the 2011 sample of the Lick AGN Monitoring Project (LAMP), Mrk 50 and Mrk 1511, using the Hβ emission line. In Section 3.3 we apply it to the Hβ and Hα emission lines for Arp 151 from the LAMP 2008 data set. In Section 4 we discuss some of the implications of this simple model for the physics of the BLR. We conclude in Section 5.

2. CARAMEL-LIGHT and CARAMEL-GAS

In this section, we first briefly describe the original code CARAMEL-LIGHT (Section 2.1) and then we describe the modifications and additional ingredients that were implemented in the CARAMEL-GAS version (Section 2.2).

2.1. A Brief Description of CARAMEL-LIGHT

A detailed description of the CARAMEL-LIGHT model including an explanation of the model parameters and the construction of the model is given by Pancoast et al. (2014b). In summary, the CARAMEL-LIGHT model consists of several (of order thousands) point particles surrounding a central black hole, which are a Monte Carlo realization of the idealized emissivity field. The positions of the particles are determined by a number of geometric parameters, and their velocities are determined by the black hole mass, particle positions, and kinematic parameters. The particles act as mirrors that instantaneously reprocess and re-emit the input continuum light curve toward the observer, where the wavelength of light re-emitted by particle i is determined by the emission line being modeled and the particle's line-of-sight (LOS) velocity. The amplitude of emission is determined by the amplitude of the continuum light curve at a time $t - \tau_i$, where τ_i is the time lag for particle i, equal to the distance from the origin divided by the speed of light. Two additional parameters rescale the particle emission: ξ (ranging from 0 to 1) describes the transparency of the BLR mid-plane and multiplies the emission from particles seen on the "far" side of the mid-plane; κ (ranging from -0.5 to 0.5) serves as an illumination function parameter where the emission of each particle is weighted by a factor $0.5 + \kappa \cos(\phi)$, where ϕ is the angle from the observer to BLR center to particle.

In general, the ionizing continuum is not available to us, so we use a proxy such as the V- or B-band continuum. The continuum and spectra fed into CARAMEL-LIGHT are rescaled so that they are in units of order unity, so the absolute fluxes are not modeled. Instead, CARAMEL-LIGHT includes two free parameters, $C_{\rm add}$ and $C_{\rm mult}$, that match the overall amplitude and amplitude of variations of the continuum and emission line data. These are incorporated into the model via the equation

$$L_i(t) = W(\xi, \phi_i, \kappa) C_{\rm mult}[C(t - \tau_i) + C_{\rm add}], \quad (1)$$

where $L_i(t)$ is the line emission of particle i at time t, $C(t)$ is the observed continuum at time t, and $W(\xi, \phi_i, \kappa)$ summarizes the effect of ξ and κ described above.

The description above is valid as long as the response of the line to variations in the optical continuum can be approximated as linear around the mean. The two constants $C_{\rm add}$ and $C_{\rm mult}$ allow for the variability of the line to have a larger or smaller amplitude than that of the continuum proxy. We note that the data only constrain the ratio between line flux and continuum

proxy, so the absolute normalization of the ionizing continuum, and therefore the ratio of the ionizing continuum to line flux, are not observables. For the same reason, the relation between the amplitude of variability of the ionizing continuum and that of the line flux cannot be constrained unless one observes the ionizing continuum directly.

2.2. From CARAMEL-LIGHT to CARAMEL-GAS: Photoionization Approximation

In CARAMEL-GAS, the point particles no longer represent BLR emission, but rather describe the distribution of physical BLR gas. As in CARAMEL-LIGHT, the particles are not meant to represent physical objects, but they are rather meant to be a Monte Carlo representation of a gas density field. As we will discuss in Section 4, interpreting them as physical objects requires additional assumptions. While those additional assumptions are not relevant for the purpose of inferring the black hole mass or the overall geometry of the gas, they are crucial for any interpretation in terms of detailed BLR physics.

To compute $L_i(t)$, we now need to know the emission properties of the gas, which depend on the incident ionizing flux and several local conditions such as the temperature, density, and metallicity. If all these values are known, the emissivity can be calculated with photoionization codes such as CLOUDY (Ferland et al. 1998). However, these computations would add prohibitive complexity to the model, which already suffers from long run times.

A simple approximation is to describe the emissivity of the BLR as a power law in radius,

$$\tilde{\varepsilon}(r) = \tilde{\varepsilon}_0 (r/r_0)^{\alpha}, \tag{2}$$

with normalization $\tilde{\varepsilon}(r_0) = \tilde{\varepsilon}_0$ (e.g., Robinson 1995; Goad et al. 2012). Goad et al. (2012) demonstrated that this is a good approximation for common emission lines such as Hβ, with $\alpha \sim -1$, by running CLOUDY models for simple slabs of gas. The grids are computed given some constant ionizing luminosity, $L_{\rm ion}$, but since reverberation mapping data deal with variable luminosities, it is useful to write Equation (2) in terms of the ionizing flux:

$$\tilde{\varepsilon}(\Phi) = \tilde{\varepsilon}_0 (\Phi/\Phi_0)^{-\alpha/2}. \tag{3}$$

To compute the line luminosity we need to make an additional assumption and assign a surface area to each point i, so that we can multiply the emissivity (erg s^{-1} cm^{-2}) by the area, $A_{c,i}$:

$$L_{{\rm line},i}(\lambda) = \tilde{\varepsilon}_0 (\Phi_i/\Phi_0)^{-\alpha/2} A_{c,i} \delta(\lambda - \lambda_i), \tag{4}$$

where Φ_i is the ionizing flux at the position of the point i. Here, we include the Dirac delta function, $\delta(\lambda - \lambda_i)$, to specify the wavelength of emission, dependent on the point's LOS velocity. We note that in terms of observables, $A_{c,i}$ is degenerate with ε_0, and therefore additional assumptions are needed if one wishes to interpret these points as physical clouds of a specific size or size distribution.

The ionizing flux is time-variable due to continuum fluctuations, so

$$\Phi_i = \Phi_i(t) = L_{\rm ion}(t - \tau_i)/4\pi r_i^2, \tag{5}$$

where τ_i is the lag between the observed continuum and cloud emission and $L_{\rm ion}(t)$ is the ionizing continuum luminosity at time t.

Combining all of the above, the total observed emission line luminosity at time t is

$$L_{\rm line}(\lambda, t) = \sum_{i=0}^{N} \tilde{\varepsilon}_0 \left[\frac{L_{\rm ion}(t - \tau_i)/4\pi r_i^2}{L_{\rm ion,0}/4\pi r_0^2} \right]^{-\alpha/2} \times A_{c,i} \delta(\lambda - \lambda_i), \tag{6}$$

where N is the number of points. Given the noted degeneracy, we will assume for simplicity that all points are the same size, and define $\varepsilon_0 = \tilde{\varepsilon}_0 A_c$:

$$L_{\rm line}(\lambda, t) = \varepsilon_0 \sum_{i=0}^{N} \left[\frac{L_{\rm ion}(t - \tau_i)}{L_{\rm ion,0}} \right]^{-\alpha/2} \left[\frac{r_i}{r_0} \right]^{\alpha} \times \delta(\lambda - \lambda_i). \tag{7}$$

The implications of this assumption are discussed in Section 4.

As discussed above, we typically do not have access to the ionizing continuum and use a proxy such as the V or B band in its place. Unfortunately, the conversion between the observed continuum and ionizing continuum is nontrivial and depends, e.g., on the spectral energy distribution (which may be time-variable), the host-galaxy subtraction, and the fact that the BLR may see a different portion of the accretion disk than the one we are able to observe. Attempting to account for these factors would introduce significant complexity to the model and require additional assumptions. Those may be desirable from the point of view of the interpretation of the results but are not necessary for the phenomenological description that is the goal of this approach. Without the observed-to-ionizing luminosity relation, any interpretation of the absolute BLR emissivity normalization will be approximate, but we can still infer the black hole mass, structural and kinematic properties of the BLR, and the radial emissivity dependence.

In practice, we assume that the BLR responds linearly to changes in the continuum and keep the additive offset used by CARAMEL-LIGHT to account for additional freedom in the relation between observed fluxes and ionizing continuum. We also account for the mid-plane transparency and illumination function utilizing the same weighting factor $W(\xi, \phi_i, \kappa)$ from CARAMEL-LIGHT:

$$L_{\rm line}(\lambda, t) = \varepsilon_0 \sum_{i=0}^{N} \left[\frac{L_{\rm obs}(t - \tau_i) + C_{\rm add}}{L_{\rm obs,0} + C_{\rm add}} \right] \left[\frac{r_i}{r_0} \right]^{\alpha} \times W(\xi, \phi_i, \kappa) \delta(\lambda - \lambda_i), \tag{8}$$

where $L_{\rm obs}$ is the observed continuum.

Finally, in order to minimize covariance between free parameters, we choose pivot points to be as close as possible to the average expectations, based on empirical information. We set r_0 equal to the BLR size determined by past reverberation mapping studies, and set $L_{\rm obs,0}$ equal to the mean continuum luminosity for the campaign.

In summary, in going from CARAMEL-LIGHT to CARAMEL-GAS we have removed one parameter, $C_{\rm mult}$, and introduced two new parameters, ε_0 and α. Based on the expectation from photoionization calculations, we use a uniform prior on α between -2 and 0. The other parameters retain the name and functions originally introduced for CARAMEL-LIGHT, but they are now to be interpreted as describing the gas distribution. We anticipate that α will be somewhat degenerate with the parameters describing the distribution of the gas density, in

Table 1
Parameter Summary

Parameter	CARAMEL-LIGHT	CARAMEL-GAS
$M_{\rm BH}$	Black hole mass	
μ	Mean BLR radius	
β	Gamma function shape parameter	
F	Minimum BLR radius, in units of μ	
θ_o	BLR half-opening angle	
θ_i	BLR inclination angle	
κ	Illumination function parameter	
γ	Disk face concentration parameter	
ξ	Mid-plane transparency	
$f_{\rm ellip}$	Near-circular orbit fraction	
$f_{\rm flow}$	Inflow–outflow parameter	
θ_e	Ellipse angle (for kinematics)	
$\sigma_{\rm turb}$	Turbulence	
$C_{\rm add}$	Additive offset (Equation (1))	Additive offset (Equation (8))
$C_{\rm mult}$	Multiplicative offset (Equation (1))	⋯
α	⋯	Emissivity power-law index
ε_0	⋯	Emissivity power-law normalization

Note. We show a summary of parameters used in CARAMEL-LIGHT and CARAMEL-GAS. In total, one parameter is removed and two parameters are added.

particular β. The parameters for the two versions of the code are summarized in Table 1.

In addition to the modifications described, there have been a few minor improvements to the CARAMEL modeling code since the results published by Williams et al. (2018) and Pancoast et al. (2014b). These changes are explained in Appendix, and tests demonstrate that the changes do not affect the modeling results.

3. Test Cases

In this section we apply CARAMEL-GAS and CARAMEL-LIGHT to a few test cases selected from the LAMP 2008 (Bentz et al. 2009; Walsh et al. 2009) and LAMP 2011 (Barth et al. 2011, 2015) campaigns, in order to achieve the following goals. First, we aim to compare the results obtained with the two approaches to test the robustness of the inferences, particularly BLR size, black hole mass, overall morphology, and kinematics. Second, we aim to interpret the results of CARAMEL-GAS in terms of the physics of the BLR. For this second goal, we focus on an AGN that has been successfully monitored in both Hα and Hβ, and attempt to use the multiline information.

3.1. Data Preparation

We look at two data sets modeled by Williams et al. (2018), Mrk 50 and Mrk 1511 from the LAMP 2011 campaign, as well as one modeled by Pancoast et al. (2014b), Arp 151 from the LAMP 2008 campaign. In each case, we use the same continuum and spectra files as used in the previous papers, except rescaled so that they are in their original physical units. The continuum light curves are expressed in erg s^{-1} cm^{-2} Å^{-1} and the spectra are converted to erg s^{-1} Å^{-1} using the luminosity distance. For Mrk 50 and Mrk 1511, the continuum is the V band whereas for Arp 151 it is the B band.

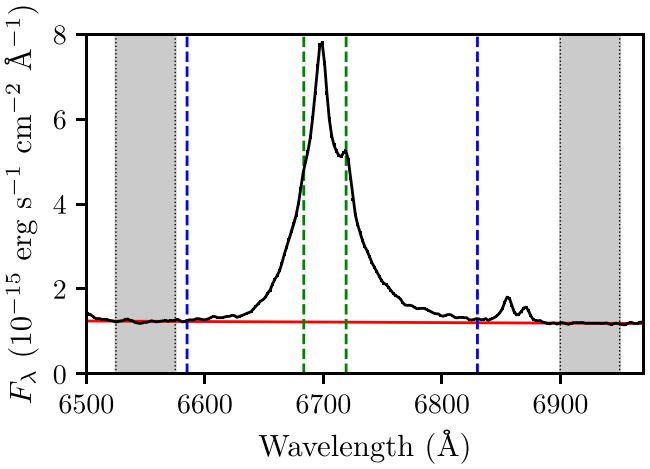

Figure 1. Example spectrum of Arp 151 showing the Hα emission line (black). The local continuum (red) was estimated by fitting a straight line between the two regions shaded in gray. The green vertical dashed lines shows the centroids of the [N II] $\lambda\lambda$6548, 6583 doublet. We model the portion of the emission line that is between the two blue vertical dashed lines.

In addition to the Arp 151 Hβ data modeled by Pancoast et al. (2014b), we also model the Hα data set from the same campaign. Bentz et al. (2010b) measured velocity-resolved lags using the Hα line and Bentz et al. (2010a) produced velocity-delay maps using the maximum entropy method, but the data have not previously been modeled using CARAMEL. The CARAMEL-GAS results will show how the inferred gas distributions and radial emissivity profiles compare for two lines of the same species.

CARAMEL-LIGHT and CARAMEL-GAS both require emission line spectra with the continuum and other contaminants removed since the BLR model only produces the broad emission line plus a narrow line component. For the three Hβ data sets, we have full spectral decompositions, and we model the data with all non-Hβ components subtracted. We do not have spectral decompositions for Hα, so the Hα data also contain, e.g., the continuum, [N II] $\lambda\lambda$6548, 6583 doublet, and galaxy starlight emission. For each epoch, we estimate a local continuum by fitting a straight line within two continuum windows on either side of Hα (Figure 1). The continuum windows are the same as those used by Bentz et al. (2010b): 6525 to 6575 Å and 6900 to 6950 Å. We also introduce an additional [N II] narrow line component to the model, which is fixed to have the same width as the Hα narrow line. the λ6548 component, $F_{\lambda6548}$, is a free parameter, $F_{\lambda6548} = F_{\lambda6583}/3$, and the lines remain unchanged throughout the duration of the campaign.

Despite these improvements, there could still be contaminant flux in the remaining spectra due to, e.g., host-galaxy starlight or Fe II emission. Additionally, the spectra are calibrated using the [O III] λ5007 line near Hβ, so the calibration at the wavelength of Hα is imperfect. Both of these factors lead to poorer fits to Hα compared to Hβ. DNEST4 includes a likelihood softening parameter—the statistical temperature,[2] T—which allows us to account for underestimated uncertainties or the inability of a simplified model to fit the data. Both the CARAMEL-LIGHT and CARAMEL-GAS runs require large values

[2] The temperature T is a statistical parameter that appears in some sampling methods and should not be confused with a physical temperature.

Table 2
Modeling Results

	Mrk 50		Mrk 1511		Arp 151, Hβ		Arp 151, Hα	
	LIGHT	GAS	LIGHT	GAS	LIGHT	GAS	LIGHT	GAS
$\log_{10}(M_{\rm BH}/M_\odot)$	$7.54^{+0.37}_{-0.28}$	$7.42^{+0.19}_{-0.18}$	$7.23^{+0.34}_{-0.24}$	$7.47^{+0.21}_{-0.39}$	$6.63^{+0.10}_{-0.10}$	$6.54^{+0.17}_{-0.12}$	$6.75^{+0.14}_{-0.08}$	$7.13^{+0.58}_{-0.22}$
$r_{\rm mean}$ (lt-day)	$8.47^{+0.64}_{-0.64}$	$10.04^{+3.81}_{-1.13}$	$6.00^{+1.80}_{-0.93}$	$9.31^{+5.59}_{-2.89}$	$3.89^{+0.31}_{-0.31}$	$5.20^{+1.62}_{-0.89}$	$6.66^{+0.55}_{-0.69}$	$9.00^{+2.13}_{-1.32}$
$r_{\rm median}$ (lt-day)	$7.03^{+0.66}_{-0.67}$	$8.63^{+3.74}_{-1.11}$	$5.19^{+1.60}_{-0.96}$	$7.61^{+5.86}_{-2.19}$	$2.52^{+0.32}_{-0.33}$	$3.47^{+1.18}_{-0.70}$	$4.94^{+0.46}_{-0.61}$	$7.16^{+2.10}_{-1.26}$
$r_{\rm min}$ (lt-day)	$0.89^{+0.99}_{-0.62}$	$0.48^{+0.42}_{-0.34}$	$1.67^{+2.09}_{-0.93}$	$1.97^{+1.96}_{-1.17}$	$0.69^{+0.34}_{-0.30}$	$0.56^{+0.29}_{-0.19}$	$0.24^{+0.20}_{-0.17}$	$0.19^{+0.22}_{-0.14}$
σ_r (lt-day)	$5.88^{+0.91}_{-0.78}$	$6.77^{+1.99}_{-0.91}$	$3.37^{+1.44}_{-1.10}$	$5.40^{+4.24}_{-2.12}$	$3.86^{+0.55}_{-0.48}$	$5.14^{+1.78}_{-0.96}$	$6.06^{+0.64}_{-0.58}$	$7.45^{+1.19}_{-1.00}$
$\tau_{\rm mean}$ (days)	$7.81^{+0.53}_{-0.56}$	$7.53^{+0.37}_{-0.40}$	$5.84^{+0.75}_{-0.64}$	$6.21^{+0.66}_{-0.77}$	$3.46^{+0.29}_{-0.28}$	$3.29^{+0.45}_{-0.34}$	$6.19^{+0.49}_{-0.59}$	$6.81^{+0.70}_{-0.64}$
$\tau_{\rm median}$ (days)	$6.10^{+0.59}_{-0.55}$	$5.72^{+0.45}_{-0.48}$	$4.77^{+0.66}_{-0.79}$	$5.00^{+0.65}_{-0.63}$	$2.07^{+0.28}_{-0.29}$	$1.82^{+0.35}_{-0.27}$	$4.23^{+0.37}_{-0.46}$	$4.85^{+0.60}_{-0.56}$
β	$0.78^{+0.14}_{-0.10}$	$0.68^{+0.09}_{-0.07}$	$0.83^{+0.30}_{-0.22}$	$0.69^{+0.61}_{-0.11}$	$1.23^{+0.17}_{-0.17}$	$1.11^{+0.18}_{-0.15}$	$0.96^{+0.06}_{-0.05}$	$0.83^{+0.07}_{-0.09}$
θ_o (deg)	$16.1^{+9.8}_{-6.1}$	$17.9^{+7.8}_{-4.3}$	$38.3^{+10.6}_{-8.9}$	$34.8^{+8.2}_{-5.5}$	$33.0^{+3.5}_{-3.5}$	$32.8^{+7.6}_{-5.9}$	$27.8^{+5.8}_{-7.5}$	$17.2^{+6.6}_{-6.7}$
θ_i (deg)	$18.8^{+9.3}_{-7.1}$	$22.0^{+7.5}_{-4.1}$	$22.3^{+9.5}_{-8.2}$	$17.6^{+11.1}_{-5.2}$	$31.2^{+2.8}_{-3.2}$	$31.0^{+5.7}_{-5.2}$	$26.0^{+4.9}_{-6.8}$	$16.1^{+5.1}_{-8.3}$
κ	$-0.09^{+0.16}_{-0.17}$	$-0.07^{+0.09}_{-0.13}$	$-0.29^{+0.36}_{-0.15}$	$-0.23^{+0.29}_{-0.19}$	$-0.43^{+0.06}_{-0.04}$	$-0.37^{+,0.07}_{-0.08}$	<-0.45	<-0.29
γ	$1.50^{+0.34}_{-0.32}$	$1.69^{+0.22}_{-0.35}$	$1.61^{+0.29}_{-0.42}$	$1.53^{+0.35}_{-0.39}$	>1.85	>1.79	$1.77^{+0.17}_{-0.26}$	$1.55^{+0.32}_{-0.31}$
ξ	$0.40^{+0.14}_{-0.20}$	$0.42^{+0.11}_{-0.16}$	$0.56^{+0.29}_{-0.24}$	$0.45^{+0.36}_{-0.39}$	$0.11^{+0.04}_{-0.04}$	$0.15^{+0.06}_{-0.05}$	$0.21^{+0.10}_{-0.06}$	$0.39^{+0.24}_{-0.16}$
$f_{\rm ellip}$	$0.38^{+0.09}_{-0.10}$	$0.39^{+0.10}_{-0.09}$	$0.67^{+0.13}_{-0.20}$	$0.70^{+0.15}_{-0.22}$	<0.06	<0.07	<0.10	<0.35
$f_{\rm flow}$	$0.75^{+0.17}_{-0.17}$	$0.75^{+0.18}_{-0.17}$	$0.61^{+0.26}_{-0.38}$	$0.63^{+0.27}_{-0.30}$	$0.25^{+0.16}_{-0.18}$	$0.26^{+0.17}_{-0.18}$	$0.25^{+0.17}_{-0.17}$	$0.27^{+0.21}_{-0.19}$
θ_e (deg)	$17.6^{+10.9}_{-11.3}$	$19.4^{+10.0}_{-11.8}$	$30.6^{+48.6}_{-22.3}$	$56.4^{+26.3}_{-45.8}$	<11.0	<13.1	<15.7	$23.9^{+16.4}_{-14.6}$
$\sigma_{\rm turb}$	<0.038	<0.023	<0.026	<0.026	<0.012	<0.016	<0.010	<0.022
$C_{\rm add}$ (10^{-15} erg s^{-1} cm^{-2} Å^{-2})	$-1.16^{+0.06}_{-0.06}$	$-1.18^{+0.04}_{-0.04}$	$-1.32^{+0.05}_{-0.05}$	$-1.33^{+0.05}_{-0.04}$	$-0.06^{+0.04}_{-0.04}$	$-0.06^{+0.04}_{-0.04}$	$0.45^{+0.14}_{-0.07}$	$0.35^{+0.09}_{-0.09}$
$C_{\rm mult}$ (10^{55} erg s^{-1} cm^{-2} Å^{-2})	$9.62^{+0.45}_{-0.40}$	...	$33.51^{+2.42}_{-2.28}$	...	$3.16^{+0.11}_{-0.10}$	...	$8.44^{+0.34}_{-0.48}$	...
α	...	>-0.72	...	$-1.02^{+0.65}_{-0.52}$	...	>-0.57	...	>-0.45
ε_0 (10^{38} erg s^{-1})	...	$0.51^{+0.06}_{-0.02}$	...	$1.94^{+2.06}_{-0.60}$	...	$0.22^{+0.02}_{-0.03}$	...	$0.70^{+0.09}_{-0.06}$

Note. Median and 68% confidence intervals are shown for each of the model parameters. In cases where the posterior PDF is one-sided, we give upper or lower limits.

of T to fit the Hα data due to the leftover contaminants and imperfect calibration.

In order to reduce parameter degeneracies, we pivot the emissivity power law around a pivot radius, r_0. This is a fixed parameter and is set based on previous reverberation mapping studies. The r_0 values we use are 5.44 and 8.66 lt-day for Mrk 1511 and Mrk 50, respectively (Williams et al. 2018); and 4.08 and 8.01 lt-day for Arp 151 Hβ and Arp 151 Hα, respectively (Bentz et al. 2010b).

Finally, we rerun each data set using the up-to-date version of CARAMEL-LIGHT, based on the model changes described in Appendix.

3.2. *CARAMEL-LIGHT versus CARAMEL-GAS*

We start by comparing the results of using CARAMEL-LIGHT and CARAMEL-GAS to model the data. Table 2 gives the median parameter values and 68% confidence intervals for each run, and Figure 2 shows the change in these values between the two codes.

The modifications to the code affect the radial emissivity of the BLR test particles, so the radial particle distribution is one of the properties one might expect to change. The emission from particles at smaller radii in CARAMEL-GAS is weighted more strongly than emission from those at larger radii, so the new model might need more particles at larger radii to reproduce the same signal at longer lags. There are slight increases in $r_{\rm mean}$, $r_{\rm median}$, and σ_r for all of the AGNs, but the increase is not statistically significant in every case. Those that have a shift greater than the 1σ uncertainties are $r_{\rm mean}$ and $r_{\rm median}$ for Mrk 50 and both Arp 151 data sets; and σ_r for both Arp 151 data sets. We do not detect any change in the minimum radius.

In contrast, the mean and median lags in CARAMEL-GAS account for the radial emissivity weighting and so are not expected to change. This is confirmed with the close agreement between the two models in every test case.

The parameter β might also be expected to change between the two models. Smaller values of β correspond to radial profiles that are near-Gaussian ($\beta \to 0$) or have a shallow drop-off $0 < \beta < 1$, whereas larger values of beta correspond to profiles that drop off rapidly with radius. Since the emissivity distribution in CARAMEL-GAS is effectively the shifted Gamma distribution of CARAMEL-LIGHT multiplied by an r^α component with $\alpha < 0$, a decrease in β would not be surprising. In most cases, the uncertainties on β are too large to detect a change, but we find a $> 1\sigma$ decrease for the Arp 151 Hα runs.

Parameters such as θ_o, θ_i, and γ describe the gas/emissivity distribution in the azimuthal and polar angle coordinates and should not be affected by the change in radial emissivity. We confirm this is the case, with all three parameter values in close agreement between the CARAMEL-LIGHT and CARAMEL-GAS models. Similarly, κ and ξ, which describe the near-side versus far-side emission, are consistent. We also find no change in BLR kinematics between the CARAMEL-GAS and CARAMEL-LIGHT models. Finally, the black hole masses should not depend on the model, and we confirm that all $M_{\rm BH}$ values are consistent for the Hβ runs, with no systematic bias between the new and old codes. We measure marginally different masses for the two Hα runs, but we suspect this is due to the calibration issues and contaminants in the Hα spectra. Introducing the [N II] component in the model improved the CARAMEL-LIGHT fits and brought the $M_{\rm BH}$ measurements into closer agreement, and it is likely that residual contaminants are influencing the CARAMEL-GAS fits for the Hα line. The CARAMEL-GAS model has more flexibility than the CARAMEL-

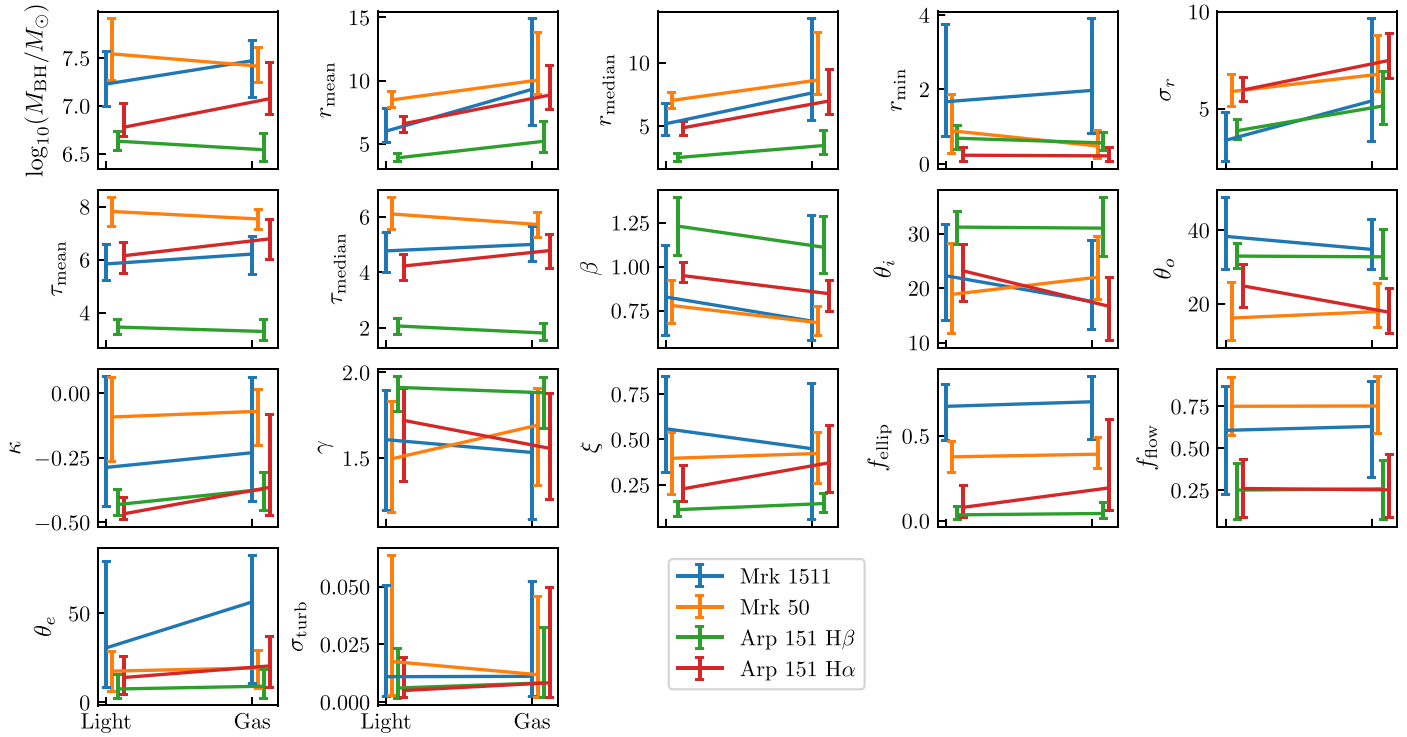

Figure 2. Parameter median values and uncertainties for the CARAMEL-LIGHT and CARAMEL-GAS models.

LIGHT model, which could allow it to explore a separate part of parameter space that better reproduces the contaminant features. Examination of the 2D posterior probability density functions (PDFs) shows that there is overlap in between the Hβ and Hα runs.

In Figure 3, we show the posterior PDFs for the parameter α in the CARAMEL-GAS runs. Both Arp 151 data sets and the Mrk 50 data prefer models with larger (less negative) α, and this parameter is poorly constrained by the Mrk 1511 data. For the Arp 151 Hα models in particular, values close to $\alpha = 0$ are strongly preferred. A value of $\alpha = 0$ would mean that there is no radial dependence of the emissivity, in which case the CARAMEL-GAS models are effectively the same as the CARAMEL-LIGHT models. However, we discuss in Section 4 the effect that our assumption of constant cloud size has on the parameter α.

3.3. Arp 151, Hβ versus Hα

We compare the modeling results for the Hβ and Hα emission lines of Arp 151. Since it is likely that both emission lines arise from the same BLR gas, we expect both models to recover the same black hole mass and the same overall geometry and kinematics. From Table 2, the black hole masses are consistent within the uncertainties for the CARAMEL-LIGHT models, but disagree at the 2σ–3σ level for the CARAMEL-GAS models. Similarly, θ_i and θ_o are consistent for the CARAMEL-LIGHT models but not for the CARAMEL-GAS models, and this is likely a result of the well documented degeneracies between $M_{\rm BH}$, θ_i, and θ_o (see, e.g., Pancoast et al. 2014b). As mentioned in Section 3.2, we suspect the tension is a result of calibration and contaminant issues in the Hα spectra. The CARAMEL-GAS model offers more flexibility than the CARAMEL-LIGHT model, and it is likely that the added flexibility allows the CARAMEL-GAS models to explore a separate part of parameter space that can better reproduce the data with the contaminants.

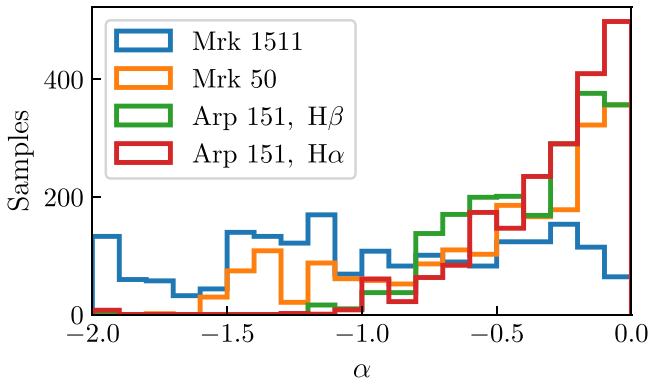

Figure 3. Posterior PDFs for α for all four CARAMEL-GAS runs. Note that the prior on α is from −2 to 0.

Examination of the 2D parameter space shows that the two posteriors do overlap, but the Hα posterior extends further down the ($M_{\rm BH}$, θ_i, θ_o) degeneracy.

The CARAMEL-LIGHT models indicate a BLR with Hα emission arising from $(r_{\rm mean}, r_{\rm median}) = (6.66^{+0.55}_{-0.69}, 4.94^{+0.46}_{-0.61})$ lt-day and Hβ emission arising from $(r_{\rm mean}, r_{\rm median}) = (3.89^{+0.31}_{-0.31}, 2.52^{+0.32}_{-0.33})$ lt-day. This stratification is visible in the BLR emissivity distributions shown in the top panel of Figure 4. In the CARAMEL-GAS models, the Hα gas distribution is still found to be at a larger radius, but the statistical significance of the gap is decreased: $(r_{\rm mean}, r_{\rm median}) = (9.0^{+2.1}_{-1.3}, 7.2^{+2.1}_{-1.3})$ lt-day for Hα and $(r_{\rm mean}, r_{\rm median}) = (5.2^{+1.6}_{-0.9}, 3.5^{+1.2}_{-0.7})$ lt-day for Hβ. It is unclear whether this is a result of the calibration issues described above or the new framework in which CARAMEL-GAS describes the BLR gas location rather than only the emission. The lags, on the other hand, remain consistent between the two models, with the Hα lag ∼3 days longer than the Hβ lag.

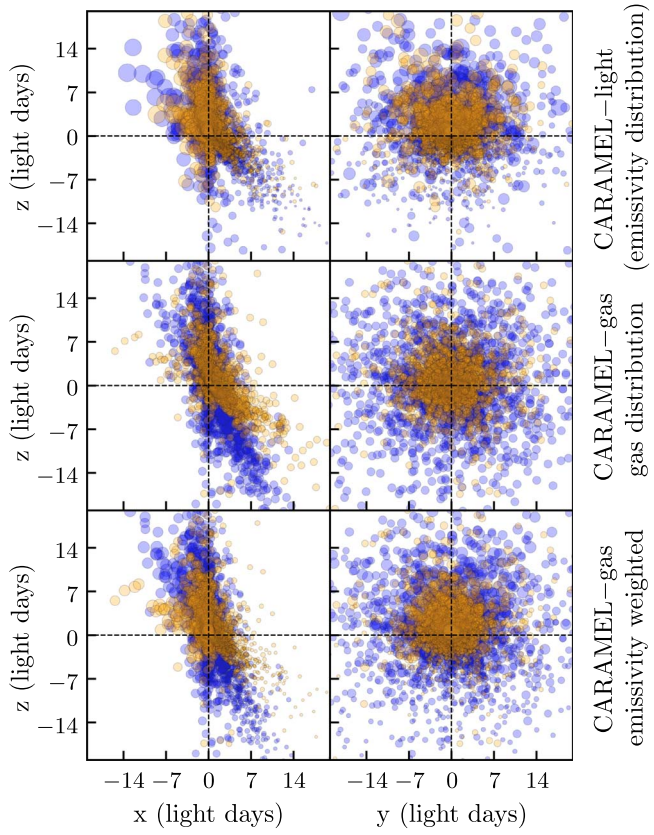

Figure 4. Geometries for the Arp 151 Hβ (orange) and Hα (blue) BLRs, where the observer is situated at $x = +\infty$. Top: emissivity distribution from the CARAMEL-LIGHT models, where the size of each point shows the relative strength of emission from the particle, determined by the parameter κ. Middle: gas distribution from the CARAMEL-GAS models. Bottom: gas distribution from the CARAMEL-GAS models, where the size of each point shows the relative strength of emission from the particle, determined by κ and the emissivity power law.

In both the CARAMEL-GAS and CARAMEL-LIGHT runs, slightly smaller values of ξ and larger values of γ are preferred for the Hβ models than the Hα models, but only ξ differs at the $>1\sigma$ level. The other asymmetry parameter, κ, is consistent between the two lines. Similarly, the kinematics are the same in all runs, with most particles on inflowing trajectories. Finally, we can only provide a lower limit on α for both the CARAMEL-GAS runs, so we do not detect any difference for the Hα and Hβ BLRs.

The panels in Figure 4 show the particle distributions for the CARAMEL-LIGHT (top) and CARAMEL-GAS (middle and bottom) models, using the parameters in Table 2. In the top and bottom panels, the sizes of the particles represent their relative strengths of emission. The close similarity between the panels illustrates the consistency between the two models, especially after the uncertainty in model parameters used to create the distributions is considered.

4. Implications

In the previous sections, we convert the BLR gas density field into an emissivity field using the power law $\varepsilon(r) \propto r^{\alpha}$. Recovering the emissivity $\tilde{\varepsilon}(r) = \varepsilon(r)/A_c(r)$ requires assumptions about the size of the gas clouds in a physical BLR. In pressure law models (e.g., Rees et al. 1989), it is common to also describe the cloud size as a power law in radius, $A_c(r) \propto r^{\alpha_{\rm size}}$, with $\alpha_{\rm size} \sim 0$ to 1.5. Combining this with the emissivity power law gives $\tilde{\varepsilon}(r) \propto r^{\alpha-\alpha_{\rm size}}$. Throughout this paper, we have been working in the special case that all clouds are the same size ($\alpha_{\rm size} = 0$), but one can also consider the more general case in which we have fit the power law $\varepsilon(r) \propto r^{\alpha}$ with $\alpha = \alpha_{\rm em} + \alpha_{\rm size}$, $\alpha_{\rm em}$ being the emissivity power-law index. Because of the degeneracy between the two parameters $\alpha_{\rm em}$ and $\alpha_{\rm size}$, it is impossible to constrain the power-law slope or the cloud size with our data. Therefore, for $\alpha = 0$ for example, we cannot distinguish whether ($\alpha_{\rm em}$, $\alpha_{\rm size}$) = (−1, 1) or ($\alpha_{\rm em}$, $\alpha_{\rm size}$) = (0, 0). However, we can proceed with the following analysis using the more general form.

As discussed in previous sections, there are other factors that make computing the emissivity of the BLR very difficult, particularly the conversion between the observed continuum and ionizing continuum. We include the parameter $C_{\rm add}$ as a simple way of allowing us to fit the data without needing to understand these complications. Looking at $C_{\rm add}$ as a fraction of the mean continuum, we find $C_{\rm add}/\overline{C} = -0.64^{+0.02}_{-0.02}$, $-0.49^{+0.02}_{-0.02}$,$-0.05^{+0.03}_{-0.03}$, $0.26^{+0.07}_{-0.07}$ for Mrk 1511, Mrk 50, Arp 151 Hβ, and Arp 151 Hα, respectively. The large values of $|C_{\rm add}/\overline{C}|$ indicate that the observed-to-ionizing continuum relation is not simply an identity or a rescaling by a constant factor for all sources. Therefore, we recommend taking the following as order-of-magnitude estimates of the emissivity.

If we treat each model particle as a spherical gas cloud with surface area $A_c(r) = A_{c,0}(r/r_0)^{\alpha_{\rm size}}$, we can place an upper limit on $A_{c,0}$ by computing the total solid angle covered by all clouds. Given an opening angle θ_o, the maximum solid angle the clouds can cover is $4\pi \sin(\theta_o)$:

$$\sum_i^N \frac{A_{c,0}(r_i/r_0)^{\alpha_{\rm size}}}{4r_i^2} \leqslant 4\pi \sin(\theta_o), \tag{9}$$

so

$$A_{c,0} \leqslant \frac{16\pi \sin(\theta_o) r_0^{\alpha_{\rm size}}}{\sum_i^N r_i^{\alpha_{\rm size}-2}}. \tag{10}$$

Therefore, the we can compute a lower limit for $\tilde{\varepsilon}_0$ for each model based on the particle distributions, θ_o, and ε_0:

$$\tilde{\varepsilon}_0 \geqslant \frac{\varepsilon_0}{16\pi \sin(\theta_o) r_0^{\alpha_{\rm size}}} \sum_i^N r_i^{\alpha_{\rm size}-2} \tag{11}$$

Using the full posterior samples for each run, we compute $\tilde{\varepsilon}_{0,\rm min}$ for a range of $\alpha_{\rm size}$ values from 0 to 1.5. The medians and 68% confidence intervals are shown in Figure 5.

Since the conditions in Mrk 50, Mrk 1511, and Arp 151 likely differ, it is hard to directly compare the Hβ results with each other. For Arp 151, however, it is intriguing to compare the emissivity parameters for the Hα and Hβ BLRs. Since the pivot points for the Hα and Hβ models are different, we compute the normalization at 5.0 lt-day and find $\log_{10}(\tilde{\varepsilon}_{0,\rm min}/{\rm erg\ s^{-1}\ cm^{-2}}) = 10.4^{+0.5}_{-0.5}$ and $12.9^{+0.9}_{-0.6}$ for Hβ and Hα, respectively, when $\alpha_{\rm size} = 0$, giving $\tilde{\varepsilon}_{0,\rm min,H\alpha}/\tilde{\varepsilon}_{0,\rm min,H\beta} \sim 300$. As $\alpha_{\rm size}$ increases, though, the ratio decreases, reaching $\tilde{\varepsilon}_{0,\rm min,H\alpha}/\tilde{\varepsilon}_{0,\rm min,H\beta} \sim 30$ when $\alpha_{\rm size} = 1.0$ and $\tilde{\varepsilon}_{0,\rm min,H\alpha}/\tilde{\varepsilon}_{0,\rm min,H\beta} \sim 8$ when $\alpha_{\rm size} = 1.5$.

In the case that both BLRs *do* cover the maximum solid angle, $\alpha_{\rm size} = 0$ would imply that the gas is *significantly* more efficient at producing Hα emission than Hβ emission in the BLR. This is unlikely based on photoionization theory, so in this case $\alpha_{\rm size}$ is likely greater than 0. Given that we find $\alpha \sim 0$

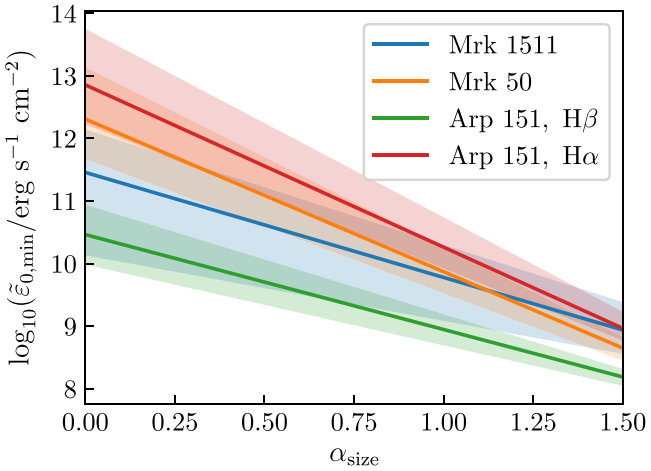

Figure 5. Median $\tilde{\varepsilon}_{0,\min}$ values and 68% confidence intervals as a function of $\alpha_{\rm size}$ for all four CARAMEL-GAS runs.

for many models, the value $\alpha_{\rm em} \sim -1$ by Goad et al. (2012) would suggest $\alpha_{\rm size} \sim 1$. However, we would need to rerun models with an expanded prior on α to determine whether α is actually greater than 0.

Alternatively, we can reduce the ratio $\tilde{\varepsilon}_{0,\mathrm{H}\alpha}/\tilde{\varepsilon}_{0,\mathrm{H}\beta}$ for a given $\alpha_{\rm size}$ by setting $\tilde{\varepsilon}_{0,\mathrm{H}\beta} > \tilde{\varepsilon}_{0,\min,\mathrm{H}\beta}$, which can be achieved if the covering factor is less than the maximum $4\pi \sin(\theta_o)$. This scenario is partially supported by the parameter γ in the Hβ BLR models, for which we find a lower limit of 1.79 compared to $\gamma = 1.55^{+0.32}_{-0.31}$ for the Hα BLR. This suggests that the gas is more concentrated near the surfaces of the thick Hβ BLR disk, and that the regions nearer the mid-plane are void of Hβ emission. More likely, we are dealing with both a lower covering factor for Hβ than Hα and $\alpha_{\rm size} > 0$.

While there are significant uncertainties in the data sets used in this paper, one with well calibrated Hα and Hβ spectra along with an observed ionizing continuum would provide more stringent constraints on $\tilde{\varepsilon}_{0,\min,\mathrm{H}\alpha}/\tilde{\varepsilon}_{0,\min,\mathrm{H}\beta}$. Paired with a more detailed functional form for $\tilde{\varepsilon}(r)$ based on photoionization calculations, the ratio could be used to measure the difference in covering factors for the Hα and Hβ BLRs.

5. Summary

We have presented a new version of the CARAMEL modeling code that models the gas distribution in the BLR and uses a simple photoionization approximation to reproduce the BLR emissivity distribution. These modifications lay the groundwork for future model development, such as the implementation of more complex emissivity laws. This is a first step toward simultaneous modeling of multiple emission lines for which data have recently become available (see, for example, the multiline data sets for NGC 5548 and Mrk 817, De Rosa et al. 2015; Kara et al. 2021).

We should note, however, that this is not a replacement for the emissivity-based version of the code, CARAMEL-LIGHT. Instead, one should select the version of the code that best addresses the relevant science case. In cases where the total energetics of the BLR are not of interest and the data for multiline modeling are not available, CARAMEL-LIGHT is the proper choice. The new parameters in CARAMEL-GAS introduce additional complexity and parameter degeneracies, so they should be avoided if not scientifically important.

The main findings of this paper are as follows.

1. The new modeling code, CARAMEL-GAS, is able to fit the observed emission line data to the same level as CARAMEL-LIGHT, introduced by Pancoast et al. (2014b).
2. The inferred values of the model parameters describing the radial distribution of particles are different in the CARAMEL-GAS runs (in which particles describe the BLR gas distribution) compared to the CARAMEL-LIGHT runs (in which particles describe the BLR emissivity distribution). The inferred time lags, which account for the emissivity law in CARAMEL-GAS, remain consistent.
3. We are unable to constrain the emissivity power-law slope for Mrk 1511, but find lower limits of -0.72, -0.57, and -0.45 for Mrk 50, Arp 151 Hβ, and Arp 151 Hα, respectively.
4. Comparing the emissivity power-law normalizations of the Hα and Hβ models suggests a lower covering factor for the Hβ BLR as well as BLR clouds that increase in size as a function of distance from the BLR center.

We would like to thank Aaron Barth, Matt Malkan, and Sandra Raimundo for helpful discussions and ideas that contributed to this work. P.W. and T.T. gratefully acknowledge support by NASA through grant HST-GO-16196 "Mapping Gas Flows in AGNs by Reverberation," by the National Science Foundation through grant AST-1907208 "Collaborative Research: Establishing the foundations of black hole mass measurements of AGN across cosmic time," and by the Packard Foundation through a Packard Research Fellowship to T.T.

Appendix A
Additional Code Modifications

Some minor changes were made to the CARAMEL-LIGHT modeling code since its publication in Pancoast et al. (2014b) and its use in the following papers: Grier et al. (2017), Pancoast et al. (2018), Mangham et al. (2019), Raimundo et al. (2019, 2020), Williams et al. (2018, 2020, 2021a), and Bentz et al. (2021). These changes have been tested and compared against the previous version of the code, and we have confirmed that all results are consistent between the two models. We have updated the code purely to simplify the model parameter space and make interpretation of the modeling results easier. All CARAMEL-LIGHT and CARAMEL-GAS runs described in this paper have implemented the following.

A.1. Geometric Construction

In the Pancoast et al. (2014b) model, the BLR geometry is constructed as follows. First, particle radii, r_j, are drawn from a shifted Gamma distribution and placed on the positive x-axis (in the direction of the observer). These particles are then rotated around the z-axis by angles $\phi_{1,j}$, drawn from a uniform distribution between 0 and 2π radians, forming a flat disk in the xy plane. Next, the particles are rotated around the y-axis by angles θ_j drawn from $\arccos(\cos\theta_o + (1 - \cos\theta_o) \times U^\gamma)$, where θ_o is the opening angle (ranging from 0 to 2π radians), γ ranges from 1 to 5, and U is the uniform distribution from 0 to 1. The particles are again rotated around the z-axis by angles $\phi_{2,j}$, also drawn from a uniform distribution between 0 and 2π, in order to form a thick disk. Finally, all particles are rotated around the y-axis by π radians minus the inclination angle, $\pi - \theta_i$, so that $\theta_i = 0$ (π) defines a face-on (edge-on) disk.

Upon close inspection, we discovered that the rotation by ϕ_2 suppressed the effect γ had on the final particle distribution, and we reformulated the construction as follows. As in the Pancoast et al. (2014b) model, particle radii are drawn from a shifted Gamma distribution, but they are then randomly placed on the positive or negative x-axis. The particles are rotated around the y-axis by angles θ_j drawn from $\arcsin(\sin\theta_o \times U^{1/\gamma})$, creating a "double wedge" in the xz plane. Next, the particles are rotated around the z-axis by angles ϕ_j drawn from a uniform distribution between 0 and 2π to create a thick disk. Finally, all particles are rotated around the y-axis by $\pi - \theta_i$ radians.

A.2. Priors

In addition to the new construction, we changed the prior limits for the following parameters:

1. γ: Using the new construction described above, γ has a stronger effect on the final particle distribution, with most of the "action" happening between $\gamma = 1$ and 2. We therefore change the prior from being uniform between 1 and 5 to being uniform between 1 and 2.
2. $\sigma_{\Theta,\mathrm{circ}}$, $\sigma_{\Theta,\mathrm{flow}}$: The particle velocities are drawn from Gaussian distributions in the v_r–v_ϕ plane, centered on the circular velocity or escape velocity (see Pancoast et al. 2014a, Section 2.5 for details). The parameters $\sigma_{\rho,\mathrm{circ}}$, $\sigma_{\Theta,\mathrm{circ}}$, $\sigma_{\rho,\mathrm{flow}}$, and $\sigma_{\Theta,\mathrm{flow}}$ define the standard deviations of these Gaussians in the radial (ρ) and angular (Θ) directions for those drawn around the circular (circ) and escape (flow) velocities. In the Pancoast et al. (2014b) model, $\sigma_{\rho,\mathrm{circ}}$ and $\sigma_{\rho,\mathrm{flow}}$ range from 0.001 to 0.1 and $\sigma_{\Theta,\mathrm{circ}}$ and $\sigma_{\Theta,\mathrm{flow}}$ range from 0.001 to 1. We found that when $\sigma_{\Theta,\mathrm{circ}}$ or $\sigma_{\Theta,\mathrm{flow}}$ is greater than 0.1, the distinction between inflow/outflow and near-circular orbits is blurred, and we therefore restrict $\sigma_{\Theta,\mathrm{circ}}$ and $\sigma_{\Theta,\mathrm{flow}}$ to fall between 0.001 and 0.1.

ORCID iDs

Peter R. Williams https://orcid.org/0000-0002-4645-6578
Tommaso Treu https://orcid.org/0000-0002-8460-0390

References

Barth, A. J., Bennert, V. N., Canalizo, G., et al. 2015, ApJS, 217, 26
Barth, A. J., Pancoast, A., Thorman, S. J., et al. 2011, ApJL, 743, L4
Bentz, M. C., Horne, K., Barth, A. J., et al. 2010a, ApJL, 720, L46
Bentz, M. C., Walsh, J. L., Barth, A. J., et al. 2009, ApJ, 705, 199
Bentz, M. C., Walsh, J. L., Barth, A. J., et al. 2010b, ApJ, 716, 993
Bentz, M. C., Williams, P. R., Street, R., et al. 2021, ApJ, 920, 112
Brewer, B. J., Treu, T., Pancoast, A., et al. 2011, ApJL, 733, L33
De Rosa, G., Peterson, B. M., Ely, J., et al. 2015, ApJ, 806, 128
Ferland, G. J., Korista, K. T., Verner, D. A., et al. 1998, PASP, 110, 761
Goad, M. R., Korista, K. T., & Ruff, A. J. 2012, MNRAS, 426, 3086
Gravity Collaboration, Amorim, A., Bauböck, M., et al. 2020, A&A, 643, A154
Collaboration, Gravity, Amorim, A., Bauböck, M., et al. 2021, A&A, 648, A117
Gravity Collaboration, Sturm, E., Dexter, J., et al. 2018, Natur, 563, 657
Grier, C. J., Pancoast, A., Barth, A. J., et al. 2017, ApJ, 849, 146
Kara, E., Mehdipour, M., Kriss, G. A., et al. 2021, ApJ, 922, 151
Mangham, S. W., Knigge, C., Williams, P., et al. 2019, MNRAS, 488, 2780
Pancoast, A., Barth, A. J., Horne, K., et al. 2018, ApJ, 856, 108
Pancoast, A., Brewer, B. J., & Treu, T. 2011, ApJ, 730, 139
Pancoast, A., Brewer, B. J., & Treu, T. 2014a, MNRAS, 445, 3055
Pancoast, A., Brewer, B. J., Treu, T., et al. 2014b, MNRAS, 445, 3073
Raimundo, S. I., Pancoast, A., Vestergaard, M., Goad, M. R., & Barth, A. J. 2019, MNRAS, 489, 1899
Raimundo, S. I., Vestergaard, M., Goad, M. R., et al. 2020, MNRAS, 493, 1227
Rees, M. J., Netzer, H., & Ferland, G. J. 1989, ApJ, 347, 640
Robinson, A. 1995, MNRAS, 272, 647
Walsh, J. L., Minezaki, T., Bentz, M. C., et al. 2009, ApJS, 185, 156
Williams, P. R., Pancoast, A., Treu, T., et al. 2018, ApJ, 866, 75
Williams, P. R., Pancoast, A., Treu, T., et al. 2020, ApJ, 902, 74
Williams, P. R., Treu, T., Dahle, H., et al. 2021a, ApJL, 915, L9
Williams, P. R., Treu, T., Dahle, H., et al. 2021b, ApJ, 911, 64